A Letters Journal Exploring the Frontiers of Physics

February 2020

EPL, **129** (2020) 34002 www.epljournal.org
doi: 10.1209/0295-5075/129/34002

Super-resolution limit of shear-wave elastography

C. Zemzemi, A. Zorgani, L. Daunizeau, S. Belabhar, R. Souchon and S. Catheline[(a)]

INSERM U1032 LabTAU, Université de Lyon - Lyon, France

received 17 September 2019; accepted in final form 10 February 2020
published online 2 March 2020

PACS 43.80.Ev – Bioacoutics
PACS 43.20.Jr – General linear acoustics: Velocity and attenuation of elastic and poroelastic waves

Abstract – When a wave field is measured within a propagative medium, it is widely accepted that the resulting image resolution depends on the measuring point density, and no longer on the wavelength. Indeed, *in situ* measurements allow the near-field details needed for super-resolution to be retrieved. Rarely studied in elastography, this is supported here by experiments. A passive elastography imaging of two inclusions in a tissue mimicking phantom is shown with a resolution down to 1/45 of a shear wavelength.

Introduction. – In optics, imaging with evanescent waves offers the possibility to overcome the classical diffraction limit of half a wavelength, with a super-resolution of near-field microscope defined by its probe size [1,2]. In the same way, a source [3–5] or a scatterer [6] smaller than one wavelength that is placed within the medium and detected in the far field also allows super-resolution. Time reversal can also overcome the diffraction limit when resonators are placed near a source [7,8], or when an acoustic sink is used [9]. To a lesser degree, near-field details can sometimes be extracted from the far field using sophisticated algorithms, such as inverse filter [10] or multiple signal classification (MUSIC) [11]. With the use of metamaterials, a super-lens, or a hyper-lens [12], moderate sub-diffraction imaging can be achieved down to a quarter of the optical wavelength. Each of these techniques uses a different approach, but they all require some near-field measurements. When a wave is measured within a propagation medium, as is often the case for surface waves in seismology, nondestructive testing, and shear-wave elastography, the diffraction limit is no longer valid. Super-resolution is inherent to these imaging techniques, and thus it only depends on the measuring point density. In elastography, the elastic wave field inside the human body is measured using ultrasounds [13,14], optics [15,16], or magnetic resonance imaging [17,18]. The general aim of elastography is to convey a palpation tomography of soft tissues to physicians. This palpation elasticity being closely related to shear elasticity, the shear-wave speed is locally estimated using different medical imaging modalities. The shear-wave field is generated using low-frequency (<500 Hz) vibrations while detection strategies are modality-dependent. In optics and ultrasounds, speckle tracking algorithms applied on successive frames acquired during the shear-wave propagation have been shown to be efficient. Elastography is thus a form of multi-wave imaging technique [19]. We will show that its resolution is limited by its smaller wavelength [20].

In this letter, a quantitative experimental estimation of the resolution in passive elastography is conducted in a tissue mimicking phantom. Passive elastography is taken as an example of shear-wave elastography. In contrast with shear-wave elastography that needs active sources, passive elastography relies on natural shear-waves due to heart beatings, muscle motions or pulsatility of arteries. The speed is estimated using noise correlation algorithms developed in the field of seismology. They were adapted in the context of medical imaging and presented here using elastodynamic equations. It should be pointed that in inert material such as that used in the following experiments, passive elastography is using active sources, vibrators, able to mimic uncontrolled wave field of living tissues. Without loss of generality, the conclusions on resolution limits are valid for any shear-wave–based elastography. Throughout experiments, the shear-wave field is kept unchanged in terms of amplitude, frequency and phase. The only parameter under consideration is the central frequency of the medical arrays or, in other words the resolution of the ultrasound imaging.

[(a)]E-mail: stefan.catheline@inserm.fr

For the sake of clarity, one last comment is worthy to be mentioned. Contrast in elastography, and thus the quantitative estimation of shear-wave speed, although important, is not the subject treated in the present paper and should not be confused with resolution.

Experimental estimation of resolution in passive elastography. – The experiments were conducted on a homemade aqueous medium. It contains gelatin (Sigma Aldrich, St Louis, MO, USA) for stiffness control and graphite (Sigma Aldrich, St Louis, MO, USA) for ultrasonic scattering. Two stiff cylindrical inclusions were embedded in a softer homogenous surrounding phantom. The gelatin concentration in the inclusion was 9% (w/v) while it was 3% (w/v) in the surrounding phantom. The graphite concentration was the same in both solutions, 0.5% (w/v). The preparation was realized in two steps. First, the solution for the surrounding phantom was prepared. Then it was poured into a mold for cooling. The mold was shaped like a truncated cylinder along elevation in order to break the symmetry of the reverberation from the boundaries, fig. 1. Two small cylinders were vertically fixed on the bottom of the mold in order to create a vacuum for the inclusion. After one hour of cooling, the inclusion solution was poured in the vacuum created by the cylinders and kept in the fridge for two more hours. The two resulting cylindrical hard inclusions have a diameter of 5 mm and are separated by 2 mm. Three shakers (RS Pro Round Speaker Driver, 1w nom, 8ω, RS Components, Singapore) that are arbitrarily positioned on the surface, emit a 0.8 s duration sweep signal from 20 Hz to 200 Hz. Simultaneously, a 128-transducer array connected to an ultrafast ultrasound scanner (Vantage® Verasonics, Inc. Kirkland, WA, USA) is used to measure the ultrasonic echoes from a homogeneous region of the soft solid. Three experiments are performed with three different arrays. Central frequencies are 5 MHz (L7-4® Philips ATL Bothell, WA, USA), 9.5 MHz (Vermon, Inc. Tours, France) and 15 MHz (Vermon, Inc. Tours, France), fig. 2(a). The axial resolution of the ultrasound images, which theoretically corresponds to $AR = (Q * \lambda)/4$ [20], is thus of the order of 154 μm, 81.05 μm, and 51.33 μm, respectively, where Q is the quality factor of the transducer, in our case $Q = 2$, and λ is the ultrasonic wavelength. In the 5 and 9.5 MHz experiment, a 15 mm coupling medium was placed between the imaging probe and the cavity to keep away the inclusion from the near field of ultrasound. Over 1 s, 1000 such ultrasound speckle images are acquired at a repetition frequency of 1 kHz using plane wave imaging [21]. The induced displacements were computed by the speckle tracking algorithm [22] from the acquired RF data. The amplitude of the displacement is $\pm 1\,\mu$m. The measured displacement central frequency is $f \sim 100$ Hz, unchanged during the three experiments. Elastic waves that are trapped in the cavity and reflected by the boundaries results in a reverberated diffuse field. For *in vivo* passive elastography, the reverberant field is produced by natural

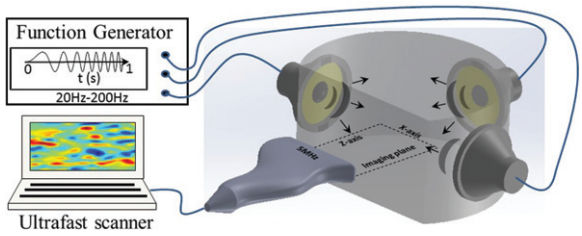

Fig. 1: Experimental set-up. The elastic diffuse field is created using three vibrators applied to random positions on the surface of the soft solid. Field measurements in the bulk require a medical ultrasound transducer array connected to an ultrafast scanner. Using speckle tracking algorithms developed in elastography, a 1 second displacement field is obtained.

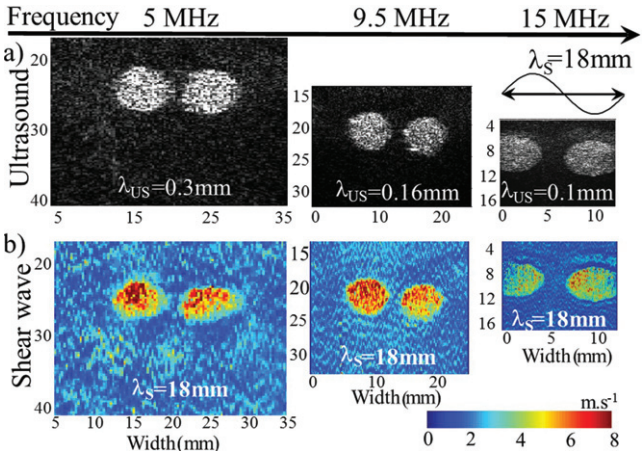

Fig. 2: The homogeneous elastic medium contains two cylindrical hard inclusions that are separated by 2 mm. (a) Ultrasound images acquired with three different arrays placed on top, with central frequencies of 5 MHz, 9.5 MHz and 15 MHz (as indicated). (b) The excellent resolution in shear-wave speed imaging using the 5 MHz, 9.5 MHz and 15 MHz probes is clearly subwavelength when compared to the 18 mm shear-wavelength representation (top right).

motion of living tissues. It is produced by muscle contractions, heart beating or arteries pulsatility. Since no shear-wave source is needed, it explains the term "passive" in the name of the technique. As usual in passive elastography, the time-reversal (TR) field is obtained through correlation of the diffuse field ϕ. For following detailed computation, see [23]:

$$\phi^{\mathrm{TR}}(r,t) = \phi(r_S, -t) \otimes \phi(r_O, t). \qquad (1)$$

The pseudo-source position is r_S, the observation point is r_O, the distance between observation and source point is $r = r_O - r_S$ and $\otimes$ stands for time convolution product. To any field that obeys the wave equation, say the particle velocity $v = \frac{\partial \phi}{\partial t}$ and the strain fields $\varepsilon = \frac{\partial \phi}{\partial r}$, one can associate general time-reversal fields $\vartheta^{\mathrm{TR}}(r,t)$ and $\xi^{\mathrm{TR}}(r,t)$. The link between $\Phi^{\mathrm{TR}}(r,t)$, $\vartheta^{\mathrm{TR}}(r,t)$ and $\xi^{\mathrm{TR}}(r,t)$ can

be computed as follows. The use of the time derivative property of a convolution product $(f \otimes g)'' = f' \otimes g'$ straightly gives:

$$-\frac{\partial^2}{\partial t^2}\phi^{\mathrm{TR}} = \frac{\partial \phi}{\partial t}(-t) \otimes \frac{\partial \phi}{\partial t}(t) = v(-t) \otimes v(t) = \vartheta^{\mathrm{TR}}. \tag{2}$$

According to this eq. (2), the time reversal velocity field ϑ^{TR} can thus be interpreted as the second time derivative of the time-reversal field or, in other words, its time curvature. As far as the time-reversal strain field is concerned, the starting point is the derivation from (1):

$$\frac{\partial^2}{\partial r_S \partial r_O}\phi^{\mathrm{TR}} = \frac{\partial \phi}{\partial r_S}(r_S, -t) \otimes \frac{\partial \phi}{\partial r_O}(r_O, t).$$

Using the variable $r = r_O - r_S$ within the time-reversal field $\phi^{\mathrm{TR}}(r_O, r_S, t) = \phi^{\mathrm{TR}}(r, t)$, the space derivative transforms to:

$$\frac{\partial^2}{\partial r_S \partial r_O}\phi^{\mathrm{TR}} = -\frac{\partial^2}{\partial r^2}\phi^{\mathrm{TR}}.$$

It finally follows that

$$-\frac{\partial^2}{\partial r^2}\phi^{\mathrm{TR}} = \frac{\partial \phi}{\partial r}(-t) \otimes \frac{\partial \phi}{\partial r}(t) = \varepsilon(-t) \otimes \varepsilon(t) = \xi^{\mathrm{TR}}. \tag{3}$$

According to this eq. (3), the time-reversal strain field ξ^{TR} can thus be interpreted as the second space derivative of the time-reversal field or, in other words, its space curvature.

On the other hand, the time-reversal field is related to the Green's function [23] according to

$$\Phi^{\mathrm{TR}}(r, t) = A\mathrm{lm}[G_{mm}(r, t)], \tag{4}$$

where A is a constant called power spectral density.

The elastic harmonic Green's function G is the solution of the elastodynamic wave equation, in a homogeneous, isotropic, frictionless solid [24]:

$$G_{mn}(r, t) = \left\{ \frac{e^{iqr}}{4\pi\rho C_p^2 r}\left[\gamma_m\gamma_n + i\frac{3\gamma_m\gamma_n - \delta_{mn}}{qr}\right] + \frac{e^{ikr}}{4\pi\rho C_s^2 r}\left[\delta_{mn} - \gamma_m\gamma_n - i\frac{3\gamma_m\gamma_n - \delta_{mn}}{kr}\right] e^{i\omega t}\right\}, \tag{5}$$

where m and n are indices of the direction axis for the source and the receiver, r is the radial distance from the source, t is the time, ρ, C_P and C_S are the density, compression wave speed, and shear-wave speed, respectively, q and k are the compression and shear-wave number, respectively, γ_i is the cosine director, and δ_{mn} is the Kronecker symbol. Let us assume that the source and the field have the same polarization, then $m = n$, $\delta_{mn} = 1$ and $\gamma_m = \cos\theta$. According to eqs. (4) and (5) the time-reversal elastic field is expressed as

$$\Phi^{\mathrm{TR}}(r, 0) = \frac{Ak}{12\pi\rho C_S^2}\left\{\left[\left(\frac{C_S}{C_P}\right)^3 (j_0(qr) + j_2(qr)) + 2j_0(kr) - j_2(kr)\right] + \left[3j_2(kr) - 3\left(\frac{C_S}{C_P}\right)^3 j_2(qr)\right]\cos^2\theta\right\},$$

where j_0 and j_2 are the first-kind Bessel functions for first and second order, respectively. In its harmonic form, time can arbitrarily be chosen equal to 0, and becomes the zero-lag time of correlation. For short-range approximation, $r \ll 1$, a linearization of the time-reversal field is computed. If the polarization of the source and of the measuring point is the same, $\gamma_m = \gamma_n = \cos\theta$, the final expression becomes:

$$\Phi^{\mathrm{TR}}(r, 0) = A\mathrm{lm}[G_{mm}(r, 0)] \approx \frac{Ak}{12\pi\rho C_S^2}\left\{\left(\frac{C_S}{C_P}\right)^3\left(1 - \frac{(qr)^2}{10}\right) + 2\left(1 - \frac{(kr)^2}{5}\right) + \frac{1}{5}\left[(kr)^2 - \left(\frac{C_S}{C_P}\right)^3 (qr)^2\right]\cos^2\theta\right\}.$$

On the source point, the distance cancels $r = 0$:

$$\Phi^{\mathrm{TR}}(0, 0) = A\mathrm{lm}[G_{mm}(0, 0)] = \frac{Ak}{6\pi\rho c_S^2}.$$

Equations (2) and (3) result in the expressions

$$\begin{aligned}\vartheta^{\mathrm{TR}}(0, 0) &= -\frac{\partial^2}{\partial t^2} A\mathrm{lm}\left[G_{mm}(0, 0)\right] \approx \frac{A\omega^2 k}{6\pi\rho c_S^2}, \\ \xi^{\mathrm{TR}}(0, 0) &= -\frac{\partial^2}{\partial r^2} A\mathrm{lm}\left[G_{mm}(0, 0)\right] \approx (2 - \cos^2\theta)\frac{Ak^3}{30\pi\rho c_S^2}.\end{aligned} \tag{6}$$

The shear-wave speed can now be extracted from the pair of eq. (6):

$$c_S = \frac{\omega}{k} = \sqrt{\frac{1}{5}(2 - \cos^2\theta)}\sqrt{\frac{\vartheta^{\mathrm{TR}}}{\xi^{\mathrm{TR}}}}.$$

In the experiments presented here, $\theta = 0$, and the speed is thus

$$c_S = \sqrt{\frac{1}{5}\frac{\vartheta^{\mathrm{TR}}}{\xi^{\mathrm{TR}}}}.$$

In order to estimate the local shear-wave speed, the origin r_0 is scanned on the whole image. Reconstruction algorithm of the shear-wave speed imaging (fig. 2) is

$$c_S(r_0) = \sqrt{\frac{1}{5}\frac{\vartheta^{\mathrm{TR}}(r_0, t_0)}{\xi^{\mathrm{TR}}(r_0, t_0)}}, \tag{7}$$

where r_0 is the position of the focal spot, t_0 is the recompression time, arbitrarily set to 0 ms.

To make the time-reversal interpretation of eq. (7) simple, the shear-wave velocity comes from ϑ^{TR} on the one hand, defined in eq. (2) as the curvature of the time recompression or, in other words, the squared central frequency, and from ξ^{TR}, on the other hand, defined in eq. (3) as the curvature of the focal spot, or in other words, the squared inverse central wavelength. To summarize, from the measurements of the 1 second displacement field $\phi(r,t)$, a numerical time derivative gives the particle velocity $v(r,t)$ and, using correlation of eq. (1), the time-reversal velocity field $\vartheta^{\mathrm{TR}}(r_S,0)$ is obtained. Similarly, a numerical gradient of $\phi(r,t)$ along depth gives the strain $\varepsilon(r,t)$ and using correlation of eq. (1), the time-reversal strain field $\xi^{\mathrm{TR}}(r_S,0)$ is obtained. Computing their ratio point by point finally gives the shear-wave speed imaging (fig. 2). Inspired by seismic noise correlation [25–28], a complete description of the elastography method is available in [23,29].

The shear-wave frequency spectrum is kept constant during the three experiments, as a constant central shear wavelength of 18 mm in the background of the medium.

Results and discussion. – When compared to conventional ultrasound imaging associated with the three frequencies (fig. 2(a)), the two inclusions are clearly apparent on the shear-wave speed reconstructions (fig. 2(b)). The 2 mm distance between the inclusions can be compared to the representation of the shear wavelength on the top right corner of fig. 2. This conveys a clear idea of what fraction of a shear wavelength the resolution of the shear-wave speed mapping can be.

The axial and lateral resolutions R_z and R_x are estimated from the average distance needed for a level inside the inclusions to decrease to the average value of the amplitude of the background (fig. 3(a)). The shear-wave speed estimation within 10% error is $2.1\,\mathrm{m\cdot s^{-1}}$, $2.0\,\mathrm{m\cdot s^{-1}}$, $1.8\,\mathrm{m\cdot s^{-1}}$ in the background and $7.1\,\mathrm{m\cdot s^{-1}}$, $6.4\,\mathrm{m\cdot s^{-1}}$, $3.6\,\mathrm{m\cdot s^{-1}}$ in the inclusions at respectively 5, 9.5 and 15 MHz. These variation estimations can be due to ultrasound SNR, or temperature changes during experiments. In any case, they are related to contrast, beyond the scope of this work, and not to resolution.

The width of inclusion edge estimation is equivalent to the -6 dB width of a point spread function. This resolution estimation is conducted on each edge of inclusion (top and side panels fig. 3(a)) for 3 consecutive profiles distributed around the center of each inclusion. Consequently, a single estimation of resolution with a relative error of 20% results from the average of 12 measurements ($3\times2\times2$) and is represented in fig. 3(b) as squares and circles. This approach is firstly validated on axial resolution of ultrasound imaging: $R_z^{\mathrm{exp}} = 140$, 80 and 50 μm are found very close to the expected theoretical values $R_z^{\mathrm{theo}} = 145$, 76 and 48 μm at, respectively, 5, 9.5 and 15 MHz.

The whole results are represented in fig. 3(b) as filled symbols for the ultrasound imaging, as open symbols for the shear-wave speed imaging, as circles for the axial resolution along z and as rectangle for the lateral resolutions along x. Although comparable at first sight on images of fig. 2, the axial resolution of the ultrasounds imaging is at least 5 fold greater than for the shear-wave speed imaging whatever the frequency, fig. 3(b). This difference comes from the speckle tracking algorithms that is used to estimate the displacement field: a windowing of five ultrasound wavelengths is responsible for the resolution degradation of the shear-wave speed imaging. The use of phase-based motion estimation [29] should make it theoretically possible for the shear-wave imaging to reach the resolution of ultrasound. As far as the lateral-resolution is concerned, no significant difference between ultrasound and shear-wave imaging is observed. It confirms that the number one limitation of resolution in these experiments is the windowing used in the speckle tracking algorithms. It should be pointed out that final resolution in shear-wave elastography is highly dependent on the strategy used for the speed estimation: noise, filtering, sampling, interpolation can become an issue. However, the results reported in the present letter clearly support the first claim that the upper super-resolution limit is independent of the shear wavelength. The best resolution reached in these experiments is 1/45 of a shear wavelength, *i.e.*, 400 μm. This super-resolution is limited by the Rayleigh criteria of ultrasound, not of the shear-waves. This is our second claim.

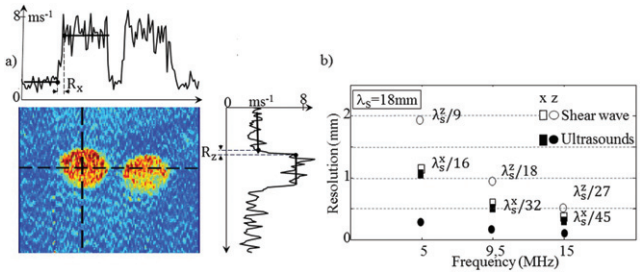

Fig. 3: (a) Profiles of inclusions, top and right panels, are extracted from the shear-wave speed reconstruction in the center. The 9.5 MHz probe is placed on top of the image. Edge length estimations provide axial R_z and lateral R_x resolution. (b) With the shear wavelength unchanged, the resolution of the shear-wave speed imaging (open symbols) follows the ultrasound imaging resolution improvement at increasing ultrasound frequencies (filled symbols). The lateral-resolution along x (rectangle symbols) reached 1/45 of a shear wavelength, *i.e.*, 400 μm.

Conclusion. – It has been shown in the first part that elastography is inherently a super-resolution technique in the sense that resolution is independent of the shear wavelength. Resolution limit as small as 1/45th of a shear wavelength is reported. Although obtained in the landscape of ultrasound passive elastography, this result is valid for any shear-wave–based imaging. As a conclusion, in the absence of noise in the data, the upper resolution bound depends 1) in ultrasound elastography [30]

on ultrasound wavelength, 2) in magnetic resonance elastography [31] on voxel size, 3) in optical coherent elastography [32,33] on light wavelength, and 4) in ultra-dense array seismology [34] on the distance between the geophones. It is worthy to stress that resolution should not be confused with contrast. These are independent concepts. Resolution rules out the separation between two neighboring points whereas contrast deals with amplitude and thus measure the ability of elastography to estimate correct quantitative shear-wave speed. Contrast problem in elastography has not been studied in the present paper.

* * *

This work is partially supported by the Marie Skłodowska-Curie Actions, Innovative Training Networks (H2020-MSCA-ITN-2014), by the Banque Publique d'Investissement (PIA, PSPC 2015), for funding of parts of this study.

REFERENCES

[1] Pohl D. W., Denk W. and Lanz M., *Appl. Phys. Lett.*, **44** (1984) 651.
[2] Hell S. W. and Wichmann J., *Opt. Lett.*, **19** (1994) 780.
[3] Lewis A., Isaacson M., Harootunian A. and Muray A., *Ultramicroscopy*, **13** (1984) 227.
[4] Dickson R. M., Cubitt A. B., Tsien R. Y. and Moerner W. E., *Nature*, **388** (1997) 355.
[5] Betzig E., Trautman J. K., Harris T. D., Weiner J. S. and Kostelak R. L., *Science*, **251** (1991) 1468.
[6] Errico C., Pierre J., Pezet S., Desailly Y., Lenkey Z., Couture O. and Tanter M., *Nature*, **527** (2015) 499.
[7] Lerosey G., De Rosny J., Tourin A. and Fink M., *Science*, **315** (2007) 1120.
[8] Rupin M., Catheline S. and Roux P., *Appl. Phys. Lett.*, **106** (2015) 024103.
[9] de Rosny J. and Fink M., *Phys. Rev. Lett.*, **89** (2002) 124301.
[10] Conti S. G., Roux P. and Kuperman W. A., *J. Acoust. Soc. Am.*, **121** (2007) 3602.
[11] Simonetti F., *Appl. Phys. Lett.*, **89** (2006) 094105.
[12] Pendry J. B., *Phys. Rev. Lett.*, **85** (2000) 3966.
[13] Krouskop T. A., Dougherty D. R. and Vinson F. S., *J. Rehabil. Res. Dev.*, **24** (1987) 1.
[14] Catheline S., Wu F. and Fink M., *J. Acoust. Soc. Am.*, **105** (1999) 2941.
[15] Razani M., Mariampillai A., Sun C., Luk T. W., Yang V. X. and Kolios M. C., *Biomed. Opt. Express*, **3** (2012) 972.
[16] Song S. *et al.*, *J. Biomed. Opt.*, **18** (2013) 121509.
[17] Muthupillai R., Lomas D. J., Rossman P. J., Greenleaf J. F., Manduca A. and Ehman R. L., *Science*, **269** (1995) 1854.
[18] Sarvazyan A. P., Rudenko O. V., Swanson S. D., Fowlkes J. B. and Emelianov S. Y., *Ultrasound Med. Bio.*, **24** (1998) 1419.
[19] Fink M. and Tanter M., *Phys. Today*, **63** (2010) 28.
[20] Righetti R., Ophir J. and Ktonas P., *Ultrasound Med. Bio.*, **28** (2002) 101.
[21] Sandrin L., Catheline S., Tanter M., Hennequin X. and Fink M., *Ultrason. Imaging*, **21** (1999) 259.
[22] Ophir J., Cespedes I., Ponnekanti H., Yazdi Y. and Li X., *Ultrason. Imaging*, **13** (1991) 111.
[23] Benech N., Brum J., Catheline S., Gallot T. and Negreira C., *J. Acoust. Soc. Am.*, **133** (2013) 2755.
[24] Aki K. and Richards P. G., *Quantitative Seismology* (University Science Books) 2002.
[25] Weaver R. L. and Lobkis O. I., *Phys. Rev. Lett.*, **87** (2001) 134301.
[26] Campillo M. and Paul A., *Science*, **299** (2003) 547.
[27] Snieder R., *Phys. Rev. E*, **69** (2004) 046610.
[28] Sabra K. G., Conti S., Roux P. and Kuperman W. A., *Appl. Phys. Lett.*, **90** (2007) 194101.
[29] Catheline S., Souchon R., Rupin M., Brum J., Dinh A. H. and Chapelon J.-Y., *Appl. Phys. Lett.*, **103** (2013) 014101.
[30] Gallot T., Catheline S., Roux P., Brum J., Benech N. and Negreira C., *IEEE Trans. Ultrason. Ferroelectr. Freq. Control*, **58** (2011) 1122.
[31] Zorgani A., Souchon R., Hoang-Dinh A., Chapelon J.-Y., Ménager J.-M., Lounis S., Rouvière O. and Catheline S., *Proc. Natl. Acad. Sci. U.S.A.*, **112** (2015) 12917.
[32] Grasland-Mongrain P., Zorgani A., Nakagawa S., Bernard S., Fitzharris G., Catheline S., and Cloutier G., *Proc. Natl. Acad. Sci. U.S.A.*, **115** (2018) 861.
[33] Zvietcovotch F., Pongchalee P., Meemon P., Rolland J. P. and Parker K. J., *Nat. Commun.*, **10** (2019) 4895.
[34] Hillers G., Roux P., Campillo M. and Ben-Zion Y., *J. Geophys. Res.: Solid Earth*, **121** (2016) 8048.